Rapid Automated Tracing and Feature Extraction from Retinal Fundus Images Using Direct Exploratory Algorithms

Ali Can, Hong Shen, James N. Turner, Howard L. Tanenbaum, and Badrinath Roysam, *Member, IEEE*

***Abstract*—Algorithms are presented for rapid, automatic, robust, adaptive, and accurate tracing of retinal vasculature and analysis of intersections and crossovers. This method improves upon prior work in several ways: 1) automatic adaptation from frame to frame without manual initialization/adjustment, with few tunable parameters; 2) robust operation on image sequences exhibiting natural variability, poor and varying imaging conditions, including over/under-exposure, low contrast, and artifacts such as glare; 3) does not require the vasculature to be connected, so it can handle partial views; and 4) operation is efficient enough for use on unspecialized hardware, and amenable to deadline-driven computing, being able to produce a rapidly and monotonically improving sequence of usable partial results. Increased computation can be traded for superior tracing performance. Its efficiency comes from direct processing on gray-level data without any preprocessing, and from processing only a minimally necessary fraction of pixels in an exploratory manner, avoiding low-level image-wide operations such as thresholding, edge detection, and morphological processing. These properties make the algorithm suited to real-time, on-line (live) processing and is being applied to computer-assisted laser retinal surgery.**

***Index Terms*—Author: please supply index terms. E-mail keywords@ieee.org for information.**

I. Introduction

OF INTEREST is the real-time tracing of the vasculature and analysis of intersections and crossovers in live high-resolution retinal fundus image sequences (1024 × 1024, 30 frames/s). Applications include montage synthesis and navigation for reliable laser surgery [1], [2], perimetry, and post-operative change detection. While the amount of work done in ophthalmic vasculature tracing is limited [1], [3]–[7], much related work has been done in X-ray angiography [8]–[30]. The present work has resulted in the adaptation, after appropriate refinements, of techniques developed for X-ray images to ophthalmology.

Real-time live ophthalmic processing presents several challenges [1], such as high image variability, the need for reliable processing in the face of nonideal imaging conditions, high data rates, and short computation deadlines. Large variability is observed between angiograms from different patients—even if healthy, with the situation worsening when pathologies exist. For the same patient, variability is observed under differing imaging conditions (see Fig. 1) and during the course of a treatment. Unlike industrial vision problems where the conditions can be carefully controlled, retinal angiograms are frequently subject to improper illumination, glare, fadeout, loss of focus, and artifacts arising from reflection, refraction, and dispersion. These effects are compounded by unavoidable body and eye movements. This is true for even the best available retinal imaging system. This issue does not arise for nonlive imaging since the photographer can capture the images when the imaging conditions are optimal. Real-time analysis calls for the handling of large volumes of data in short periods of time. Even as computing speeds increase, it is likely that the data rates will continue to stress image computing systems as frame rates, image sizes, number of bits per pixel, and potentially, the number of spectral channels [31], [32], inevitably grow in the future. This paper presents algorithms that are not only adaptive enough to be useful and reliable but are also efficient enough to handle the high data rates of interest, even on standard workstations.

II. Background

Broadly, two approaches exist for vasculature analysis. One approach [3]–[6], [8], hereafter referred to as the "pixel-processing approach," works by adaptive filtering or segmentation, followed by thinning and branch point analysis. These methods require the processing of every image pixel and numerous operations per pixel. When these operations are highly regular, they may be implemented on fast workstations [8] and pipelined accelerators [6]. Some artificial intelligence methods also require similar methods for preprocessing [9]–[11]. Generally, these methods scale poorly with image size and are unable to provide useful partial results if a computational deadline occurs.

The second approach, exemplified by this paper and several others [8], [12], is referred to as vessel tracking, vectorial tracking, or tracing. These methods work by first locating an initial point and then exploiting local image properties to trace the vasculature recursively. They only process pixels close to the vasculature, avoiding the processing of every

Manuscript received xxxx; revised xxxx. This work was supported by the National Science Foundation under Grant MIP-9412500 and Grant MIP-9634206.

A. Can, H. Shen, and B. Roysam are with the Electrical and Computer Science Engineering Department, Rensselaer Polytechnic Institute, Troy, NY 12180-3590 USA (e-mail: roysam@ecse.rpi.edu).

J. N. Turner is with the ECSE Department, Rensselaer Polytechnic Institute, Troy, NY 12180-3590 USA and also with the Wadsworth Center for Laboratories and Research, NYS-DOH, Albany, NY 12201-0509 USA.

H. L. Tanenbaum is with The Center for Sight, Albany, NY 12204 USA.

Publisher Item Identifier S 1089-7771(99)01796-3.

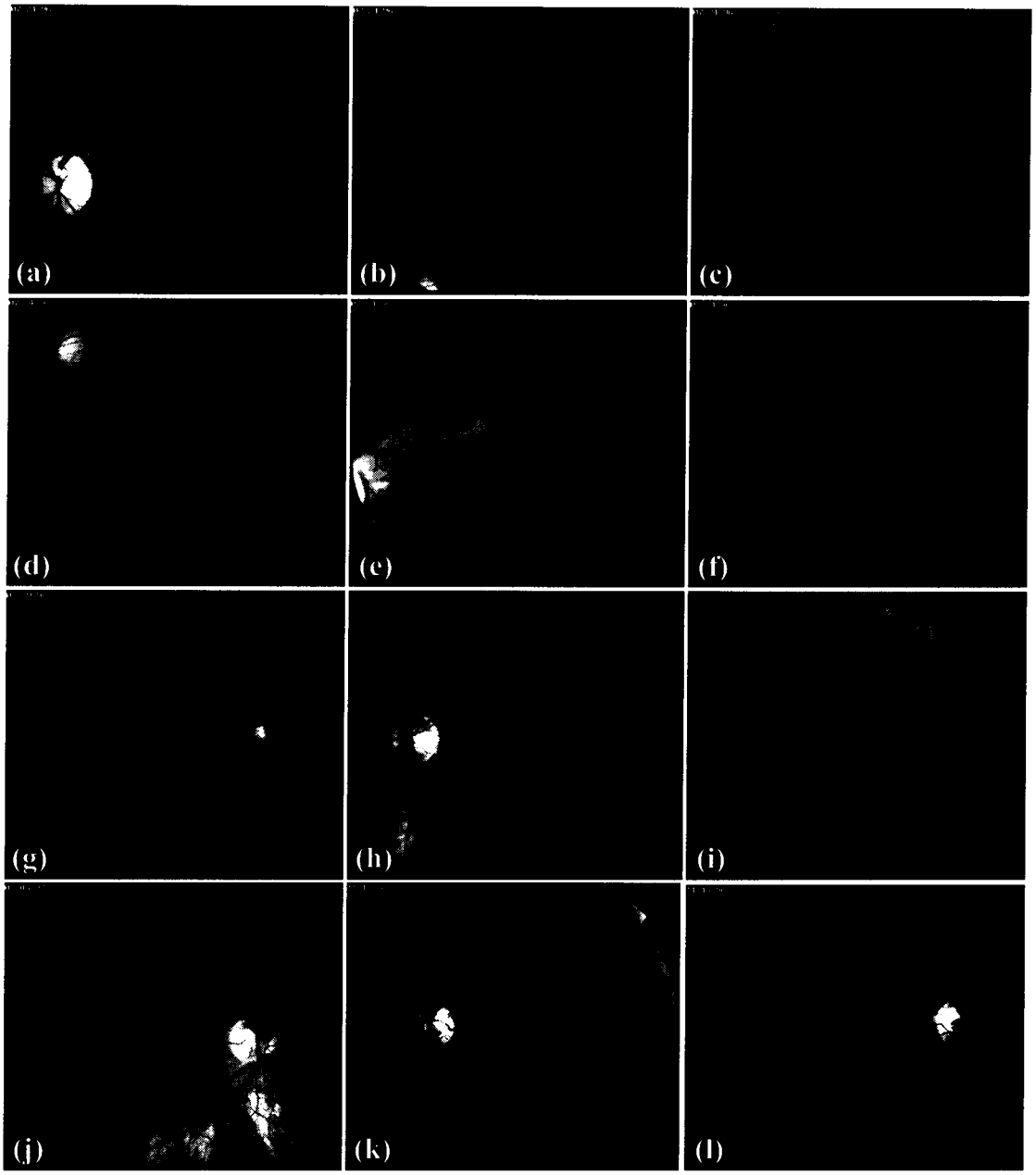

Fig. 1. Sample live retinal video angiograms from healthy (upper two rows) and pathologic eyes (lower two rows) from different patients, illustrating image variability. When controlling a surgical tool in an on-line system, it is necessary to be able to process as many frames as possible and to be able to detect frames that were not processed satisfactorily.

image pixel, and so are appropriately called "exploratory algorithms." They have several properties that make them attractive for real-time live high-resolution processing, since they scale well with image size, can provide useful partial results, and are highly adaptive while being efficient. As an aside, numerous papers have been published on vectorization of binarized images within the document image processing literature [33]. Also, a parameterized variation of the tracing approach, known as "snakes" [13], [21], is not considered here since it is unattractive for tracing branched structures due to problems with initialization.

Broadly, three exploratory processing techniques are described in the literature. In the first technique, commonly used in quantitative coronary analysis (QCA), the initial and end points of the vessel (sometimes also the direction and width) are entered manually [14]–[23]. Although these algorithms are very accurate, they are unsuitable for real-time retinal image processing since they require manual input and suffer from high computational time, which are not compelling constraints in QCA. In the second technique, the algorithm starts with a manually-entered initial point and an initial direction, and recursively tracks the entire arterial tree [24], [25], using a breadth-first search. This would not be useful for retinal images since the vessels are not necessarily connected, especially in partial views. In the third technique, the algorithms automatically extract the vascular tree without intervention. They work well for coronary angiograms and have been applied to three-dimensional (3-D) reconstruction [34]–[37]. Most of

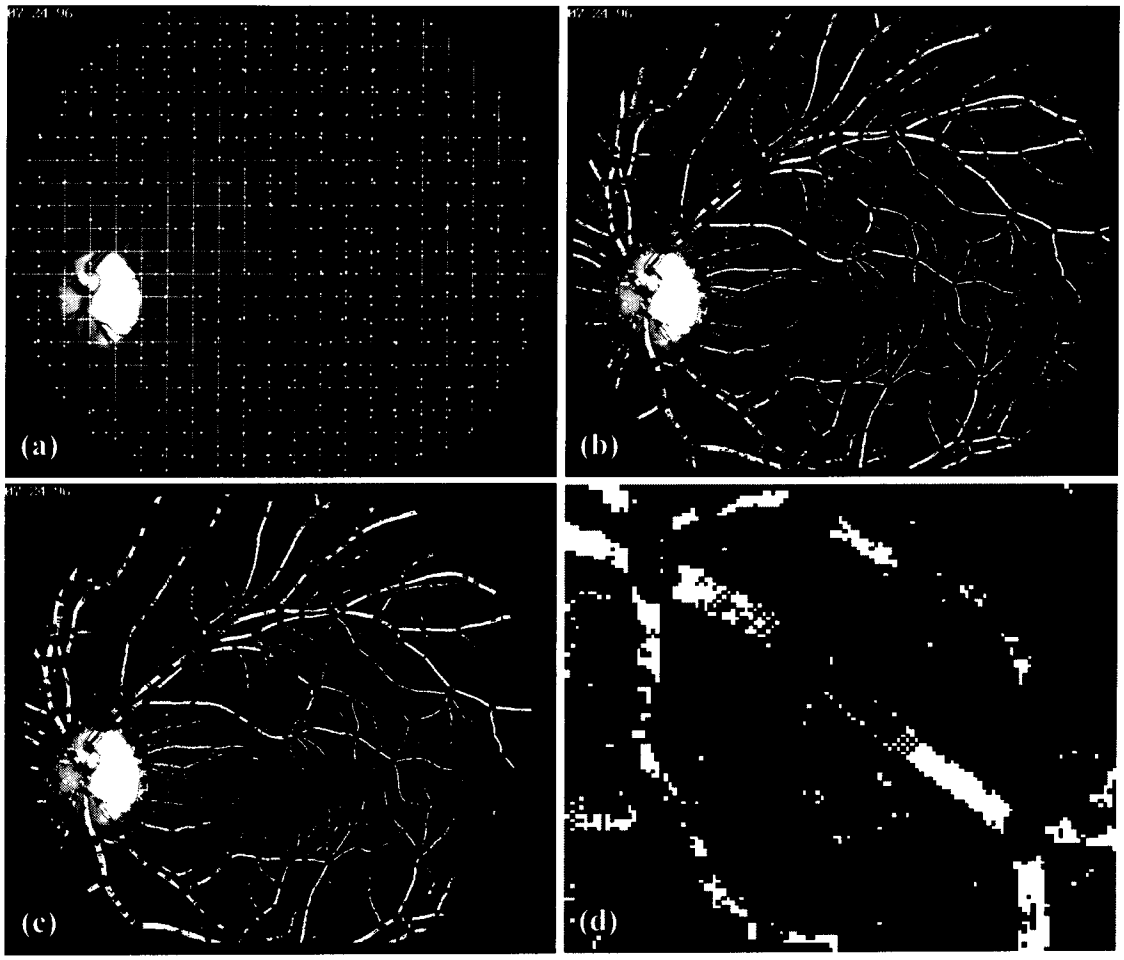

Fig. 2. (a) Grid search for seed points. Dots indicate detected local minima. (b) A result of running the validation rules for every pixel in the image. Straight portions of vessels, and portions that are not "hollow" [e.g., boxed region in (c)] are detected. (c) Points in (b) that resulted in more than 10 iterations. (d) Enlarged view of the boxed region in (c). Fig. 8 shows that the algorithm is not affected by such regions.

the techniques [26]–[29] utilize the centerline gray-level intensities. In retinal angiograms, although the blood vessels are darker than the local background, areas like the fovea are also dark relative to the average background. This consideration has motivated us to develop algorithms that rely on more localized cues, such as contrast and edge gradients, similar to some of the methods used in QCA [17]–[19]. This choice also enables our algorithms to be more robust to lighting related artifacts such as glare, dropouts, and overexposed frames which can easily occur in retinal images, especially the pathological ones of most interest.

The algorithm of Collorec and Coatrieux [26] is most closely related to the present work. Indeed, this work overcomes two "hard problems" described by Coatrieux *et al.* [12], namely: 1) robust and accurate handling of branching and crossover points and 2) improved handling of discontinuous regions by relying on local contrast, and edge information (as opposed to gray values), instead of a global intensity threshold. It also overcomes their "looping" artifact by using an improved stopping criterion. Some tracing accuracy improvement is also gained by more accurate angular discretization, more filtering across and along the vessels, and more careful handling of the discrete image space. Computationally, our algorithm is comparably attractive. The strict rules used by our algorithm for validation and verification of initial seed points allows it to reject many artifactual seed points, making up for the higher complexity in the core tracing computations.

III. Methods

Fig. 1 shows some sample images exhibiting typical variations in brightness, contrast, the presence of imaging artifacts, and pathologies. Nevertheless, it can be assumed that vessels have a lower reflectance compared to the local background. Also, they have well-defined edges, and the intensity within the vessels varies smoothly. Finally, the vessels are locally continuous, and changes in direction between branching points are smooth. It is expected that the vessels are not all connected since the image in question could represent a partial view. Occasionally, portions of vessels may appear hollow, somewhat similar to stenoses in X-ray images [Fig. 2(d)] due to certain pathological, blood flow, or imaging conditions. Finally, it is assumed that the images are corrupted minimally by Gaussian noise.

The tracing method is based on adaptive exploratory processing of the image, directly at the image intensity level, without preprocessing, avoiding image-wide pixel-processing

operations such as filters, edge operators, morphological filters, and segmentation. Each stage of the algorithm is designed to identify and restrict the computations to only the most relevant and promising locality of pixels. The computations themselves are all performed in fixed-point arithmetic using mostly local shift and add operations. The first step of the algorithm explores the image along a grid of one-pixel-wide lines, estimating the frame contrast and brightness levels, and seeking out local gray-level minima [Fig. 2(a)]. Prior to using any of these minima as a seed point for tracing, they are tested for validity using a set of strict validation and verification rules, described in Section III-E. The second step of the algorithm is a sequence of exploratory searches initiated at each of the validated seed points. Specific mechanisms are used to pool the results of the many exploratory searches, and to avoid repeated searches described further in Section III-F. Mechanisms are also described to detect critical points such as vessel crossovers, branch points, and end points (see Section III-G).

A. Directional Matched Low-Pass Differentiator Templates

The core tracing algorithm is based on the use of a set of two-dimensional (2-D) correlation kernels that act as low-pass differentiators [37] perpendicular to the direction of the vessels, and low-pass averaging filters along the vessel. For instance, a part of a blood vessel that is locally oriented along the x axis [Fig. 3(a)] can be detected using the peak response of the following correlation kernel:

$$h(x, y) = \frac{1}{8K}\{-\delta(y-2) - 2\delta(y-1) + 2\delta(y+1) + \delta(y+2)\} \otimes \left\{\sum_{k=0}^{K-1} \delta(x-k)\right\} \quad (1)$$

where $\otimes$ represents a convolution operator in the y direction. In this paper, a kernel of the above form with $K = 6$ was used. For computational efficiency, the constant factor was dropped. With this, the computation only involves fixed-point shift and add operations. For convenience of exposition, the templates in Fig. 3 are grouped as left and right templates. The left templates find the edge location in the 90° counterclockwise direction, and similarly right templates are tuned to the right boundary. The thick arrow in Fig. 3 indicates the sense of the templates. The location $\vec{p}^k$ at the base of the arrow indicates the point on the vessel centerline at which the template is computed.

Vessel boundaries at arbitrary angles can be detected by kernels that are obtained by rotating (1). An exact rotation would yield fractional weights, and the computational advantages of the above kernel would be lost. This motivated an exhaustive search for kernels that approximate the ideally rotated template in (1), using weights of 1 and 2, and meeting the constraint that the sum of the squares of the weights are the same for any angle. The latter constraint ensures that, when multiple templates are correlated at a point on the boundary of a vessel, the one that is closest to the direction of the blood vessel also produces the highest response. This search yielded a set of templates which for $K = 6$, had the angular quantization error, i.e., the angle between the gradient estimate computed for the template, and the corresponding ideal direction (one of 16 possible) of no more than 1°. For the templates in Fig. 3, the angles of rotation are discretized to 16 values, separated by 22.5°, and each template has the same sum of squared weights value of 60. They can be computed using fixed-point addition and shift operations alone, without multiplications.

The above design is neither unique nor optimal. In principle, it is desirable to select the kernels so that they function as matched filters [14]. Such an optimal design was avoided in this work in favor of a suboptimal but computationally advantageous design.

B. Application of the Templates to Recursive Tracing of Vessels

Starting from a point $\vec{p}^k$ and an initial orientation s^k on a vessel, the templates can be used to estimate the next point on the vessel $\vec{p}^{k+1}$ and its orientation s^{k+1} in a recursive manner, where the superscript k is the iteration number, with $k = 0$ specifying the seed point [see Fig. 4(a)]. The procedure for obtaining the seed points automatically is described in Section III-E. Let $\vec{u}^k$ denote a unit vector along the blood vessel at point $\vec{p}^k$. Since the directions are quantized, it is helpful to refer to directions by their indices. Specifically, if s^k is an index, assuming values from the set $\{0, 1, 2, 3, \cdots, 15\}$, into the 16 quantized directions, then the unit vector $\vec{u}^k$ can be written as follows:

$$\vec{u}^k = \begin{bmatrix} u_x^k \\ u_y^k \end{bmatrix} = \left[\cos\left(\frac{2\pi s^k}{16}\right) \sin\left(\frac{2\pi s^k}{16}\right)\right]^T. \quad (2)$$

Denote the right and left templates in the direction s as T_R^s and T_L^s, respectively. Let $R(x, y, s)$ and $L(x, y, s)$ denote the correlations between the image data $I(x, y)$, and the right and left templates in direction s, respectively, i.e., the "template responses,"

$$R(x, y, s) = \sum_{n,m}\sum I(x+n, y+m)T_R^s(n, m) \quad (3)$$

$$L(x, y, s) = \sum_{n,m}\sum I(x+n, y+m)T_L^s(n, m). \quad (4)$$

Given the current position $\vec{p}^k p^k$ and the direction s^k, the right and left templates are correlated with the local image data at pixels starting from $\vec{p}^k$ along the two directions perpendicular to the unit vector $\vec{u}^k$, respectively. For the hypothesized direction s^k, the right and left edge locations are estimated to be at the locations where $R(x, y, s)$ and $L(x, y, s)$ are maximum. The search for the maximum is limited to a distance $M/2$ in each direction, where M is the maximum expected width of a blood vessel. A value of 26 pixels was used in our work based on measurements from numerous images. For each given direction s^k, the above search produces two numbers. $R_{\max}(s^k)$ is the maximum value of the template response, and $d_R(s^k)$ is the distance from the centerline at which the maximum response occurs. Mathematically

$$R_{\max}(s^k) = \max_{d=0, 1, 2, \cdots, M/2}\{R((p_x^k + du_y^k), (p_y^k - du_x^k), s^k)\} \quad (5)$$

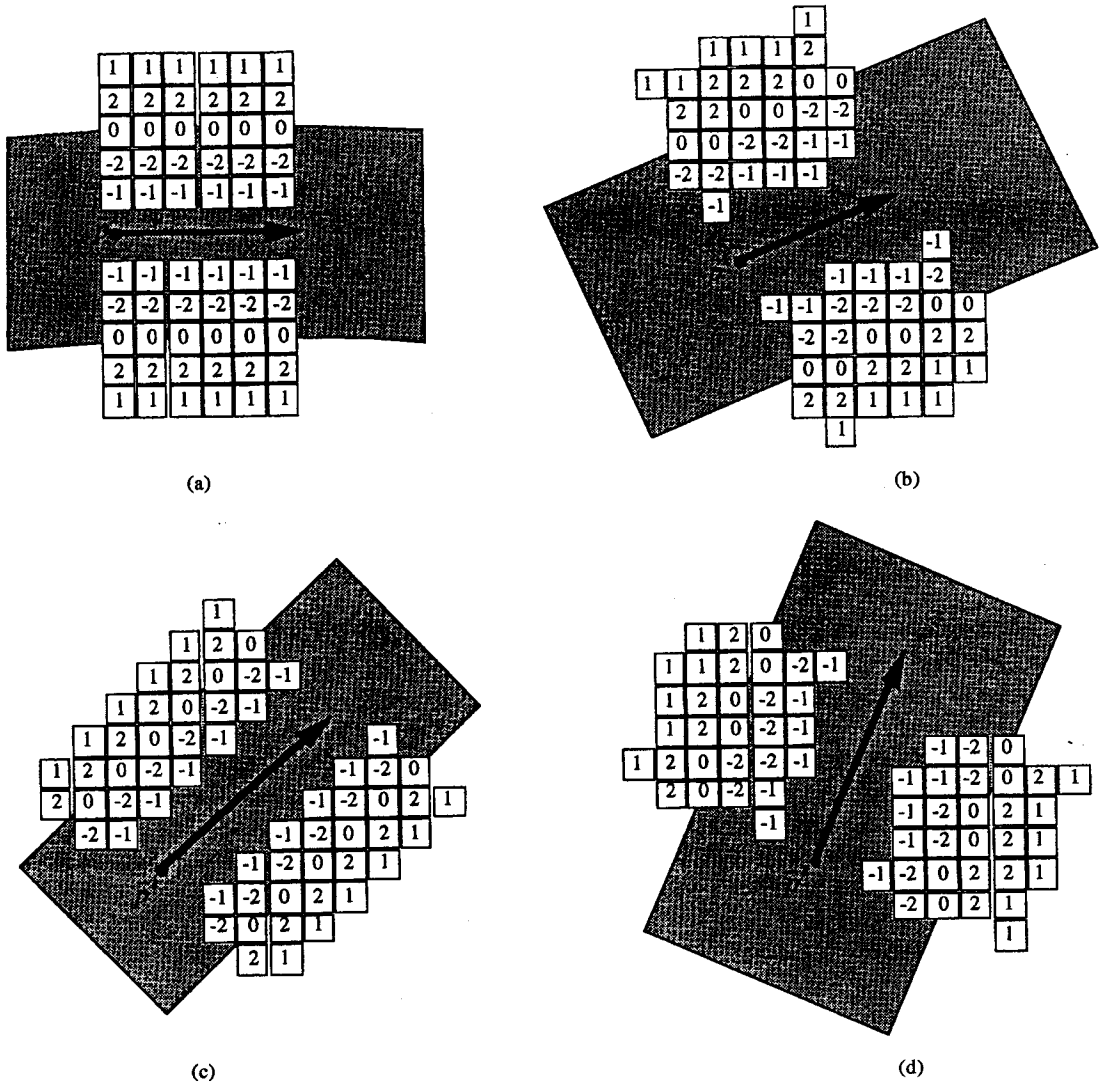

Fig. 3. Right and left templates at 0°, 22.5°, 45°, and 77.5°. The shaded region represents a hypothetical vessel oriented along the template. The thick arrow shows the sense of the templates, and $\vec{p}^{\,k}$ indicates the point on the vessel centerline at which the template is computed.

$$d_R(s^k) = \underset{d\in\{0,1,2,\cdots,M/2\}}{\operatorname{argmax}} \{R((p_x^k + du_y^k), (p_y^k - du_x^k), s^k)\}. \quad (6)$$

The corresponding quantities for the other direction are defined similarly and are denoted $L_{\max}(s^k)$, and $d_L(s^k)$, respectively. To track possible changes in the direction of the vessel, the above procedure could be repeated with s^k replaced by 15 other directions. However, if the changes in direction between crossover and branch points are known to be smooth, then just the neighbor directions may be used. So, the tracing algorithm computes the new direction s^{k+1} as shown in (7), at the bottom of the page.

The inner max operation is aimed at handling branching and crossover points. With this formulation, the tracing follows the strongest edge at these points. With (7), one can estimate the new position vector as

$$\vec{p}^{\,k+1} = \vec{p}^{\,k} + \alpha\vec{u}^{k+1} \quad (8)$$

where α is a step size. Although intuitive, the above algorithm has a drawback that results from the coarse angular discretization (22.5°). Small changes in direction, say 5°, can go unaccounted for, resulting in "jaggy" looking estimates. This problem can be overcome by exploiting the precise locations of the estimated left and right boundaries. This information is captured in the form of a "refinement vector," denoted $\vec{\beta}^{k+1}$, whose purpose is to adjust the location of the center point $\vec{p}^{\,k+1}$ based on the estimates $d_R(s^{k+1}$, and $d_L(s^{k+1})$,

$$s^{k+1} = \underset{s\in\{(s^k-1)\bmod 16,\, s^k,\, (s^k+1)\bmod 16\}}{\operatorname{argmax}} \{\max\{R_{\max}(s),\, L_{\max}(s)\}\} \quad (7)$$

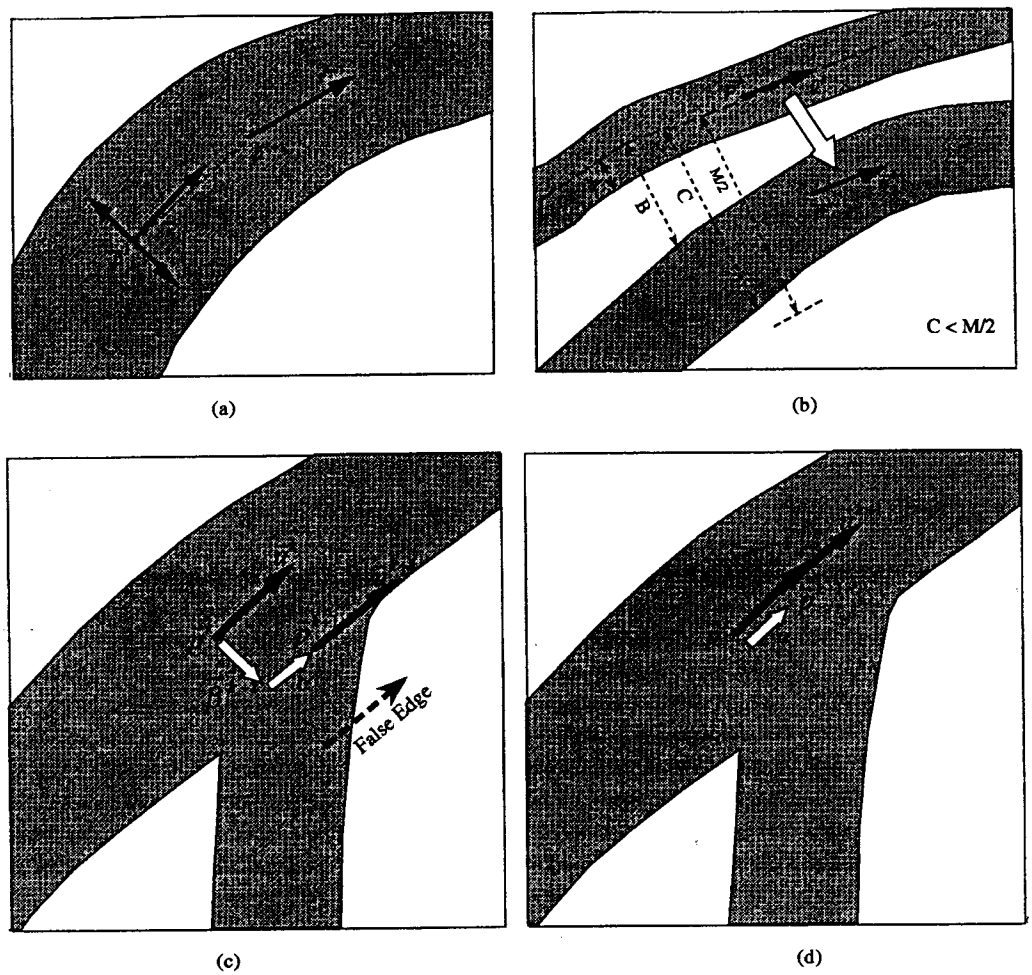

Fig. 4. (a) The iterative tracing procedure. (b) Failure of (8) for closely situated vessels. (c) Special handling of branch points by simply suppressing the refinement vector at such points, as illustrated in panel (d).

as shown below:

$$\vec{\beta}^{k+1} = \begin{bmatrix} \beta_x^{k+1} \\ \beta_y^{k+1} \end{bmatrix} = \frac{1}{2} \begin{bmatrix} (d_L(s^{k+1}) - d_R(s^{k+1}))u_x^{k+1} \\ (d_R(s^{k+1}) - d_L(s^{k+1}))u_y^{k+1} \end{bmatrix}. \quad (9)$$

With the refinement vector, the modified recursion is given by

$$\vec{p}^{k+1} = \vec{p}^{k} + \vec{\beta}^{k+1} + \alpha \vec{u}^{k+1}. \quad (10)$$

These computations can be implemented efficiently by noting that $d \in \{0, 1, 2, \cdots, M/2\}$ and $s^k \in \{0, 1, \cdots, 15\}$ are from small sets of integers. Look-up tables can be used to precompute and store the trigonometric functions in (2), after scaling by d, and rounding off to integers. This further avoids the need for floating-point computations.

C. Stopping Criteria

The tracing is terminated if one or more of the following conditions are satisfied.

1) The new point $\vec{p}^{k+1}$ is outside the image field.
2) A previously detected vessel intersects the current one. All the pixels connecting the points $\vec{p}^{k}$ and $\vec{p}^{k+1}$ are checked for this test, which is detailed in Section III-F.
3) The sum of the left and right template responses is below a sensitivity threshold T, i.e.,

$$R_{\max}(s^{k+1}) + L_{\max}(s^{k+1}) < T. \quad (11)$$

The threshold T is estimated adaptively for each image frame based on the dynamic range of its grayscale values (see Section III-H). The outputs of the templates depend on the gray-level contrast of the image field, so for a fixed sensitivity threshold T, the stopping criterion in (3) terminates the tracing algorithm earlier for low-contrast images than for high-contrast ones. This may result in some undetected vessel segments in dark images and extra false detection in bright images.

D. Modifications for Handling Jumps and Branches

If some vessels run close to each other [see Fig. 4(b)], specifically, if the furthest edge of one vessel is closer than $M/2$ pixels from the center of the other vessel, the tracing algorithm can "jump" from one vessel to the other if the other vessel has a higher template response. Furthermore, at branch points [illustrated in Fig. 4(c)], one of the edges is not parallel to the other, so this may induce an unwanted deviation in the tracing algorithm. The above two situations are handled with minor modifications to the core tracing algorithm, as described below.

1) Jumps Between Vessels: These can be prevented by terminating the search in (5) and (6) when the other vessel's edge is detected. With reference to Fig. 4(b), if a search is initiated at point $\vec{p}^k$ in a direction perpendicular to $\vec{u}^k$ then it encounters a peak response for the right template at a distance of approximately "A," and then a negative peak response at a distance of approximately "B." The latter peak is approximately the same as the response of a left template with the sign reversed. Now, the sensitivity threshold in (11) is designed such that it is exceeded by the sum of the left and right template responses whenever a valid vessel boundary is detected [see (11)]. This motivates the following criterion for terminating the search in (5) and (6). If m denotes a point along the search line, where $m \leq M/2$, the search is terminated for the right templates if

$$\max_{d=0,1,2,\cdots,m} \{R((p_x^k + du_y^k), (p_y^k - du_x^k), s^k)\} - R((p_x^k + (m+1)u_y^k), (p_y^k - (m+1)u_x^k), s^k) > T. \quad (12)$$

The criterion for terminating the search in the other direction is analogous.

2) Unwanted Deviations at Branching Points: Although the algorithm for selection of the new direction s^{k+1} operates correctly at branching points, the mechanism for selecting the new point $\vec{p}^{k+1}$ does not. As illustrated in Fig. 4(c), the right template is matched to a false boundary at the branching of the vessel. In this case, the refinement vector $\vec{\beta}^{k+1}$ introduces significant error at branching points, so the next point $\vec{p}^{k+1}$ can be computed more accurately by simply suppressing the refinement vector, and using (8) instead of (10) at branching points [Fig. 4(d)]. To implement this switching between two formulas, a criterion is needed to detect branching points.

At the branching points, while the output of the template that is matched to the true boundary in the estimated direction s^{k+1} is high, the output of the template matched to the false boundary is usually low, since the direction of the branching side vessel is different from s^{k+1} [see Fig. 4(c)]. This motivates the following test. A point is declared as a branch/crossover if

$$|R_{\max}(s^{k+1}) - L_{\max}(s^{k+1})| > \rho |R_{\max}(s^{k+1}) + L_{\max}(s^{k+1})| \quad (13)$$

where ρ is a fixed threshold. The absolute value of the above ratio is used since the branching can occur on either side. In our work, the threshold ρ is chosen as 1/3, i.e., when the response of the false boundary is half of the response of the true boundary. The above test is only performed when the estimated directions of the left and right boundaries are different.

E. Automatic Selection of the Initial Points and Directions

This section presents an automatic two-step method based on grid analysis for estimating the initial seed points and the initial directions. The first step is similar to the procedure used by Collorec and Coatrieux [26]. The second step represents an improvement.

Step 1—Line Searches over a Coarse Grid: Ideally, if the vessels in an image were all connected, the tracing algorithm would need to be initiated at just one point. However, this condition is not met in retinal angiograms. Furthermore, the tracing algorithm described above is designed (for computational reasons) to follow the strongest edge whenever a branch point is encountered, rather than performing a breadth-first search on the vasculature. For these reasons, the tracing algorithm is initiated at several points, and the traces are combined. The seed points are identified by performing a set of $2N$ line searches over the image, using a set of grid lines as illustrated in Fig. 2(a). The gray-level values on each line are low-pass filtered using a discrete approximation (0.25, 0.5, 0.25) to a one-dimensional (1-D) Gaussian kernel. This kernel is computationally attractive, since it is composed only of local fixed-point shift and add operations. Local intensity minima are detected [indicated by dots in Fig. 2(a)] on this line using a neighborhood size N_s, using a 1-D sliding window. Small values of N_s are needed to detect thin vessels. However, this leads to the detection of multiple local minima on thick vessels. To prevent this, N_s must be chosen to be equal or higher than the widest expected vessel, i.e., M. In our work, $N_s = M$. With this, the number of detected local minima as a function of the grid size N is plotted in Fig. 5(a). Clearly, better schemes may be devised for setting the neighborhood size, depending upon the application of interest. For instance, N_s may be adjusted upwards for sparse grids to improve the detection of short vessels. From a computational standpoint, Step 1 is extremely fast. Furthermore, it can be structured so as to overlap with image input/output.

Step 2—Filtering the Results of Step 1: Some of the local minima detected in Step 1 may correspond to noise and must be rejected to avoid unnecessary tracing. The directional templates provide a powerful mechanism for performing such filtering and, additionally, provide estimates of initial directions for tracing. If a seed point $\vec{p}^0$ is on a locally straight vessel segment with an unknown direction $\vec{u}^0$, note that it should yield high template responses in a pair of oppositely oriented directions of the form s^0 and $(s^0 + 8) \bmod 16$ in a small neighborhood of $\vec{p}^0$. On the other hand, the template responses are expected to be low in directions perpendicular to the orientation of the vessel. These observations lead to the following validation rules for selecting reliable seed points.

1) The outputs of the right templates in all 16 directions must have two local maxima.
2) The directions between the local maxima computed in 1) must differ by $180° \pm 22.5°$.
3) The outputs of the left templates in all 16 directions must have two local maxima.
4) The directions between the local maximum computed in 3) must differ by $180° \pm 22.5°$.
5) The directions between the local maxima computed in 1) and 3) should differ by $\pm 22.5°$.
6) The sum of local maxima computed in 1) and 2) should exceed the sensitivity threshold T.

The above rules are not applied to all seed points. They are only applied selectively, as described in the next section. They

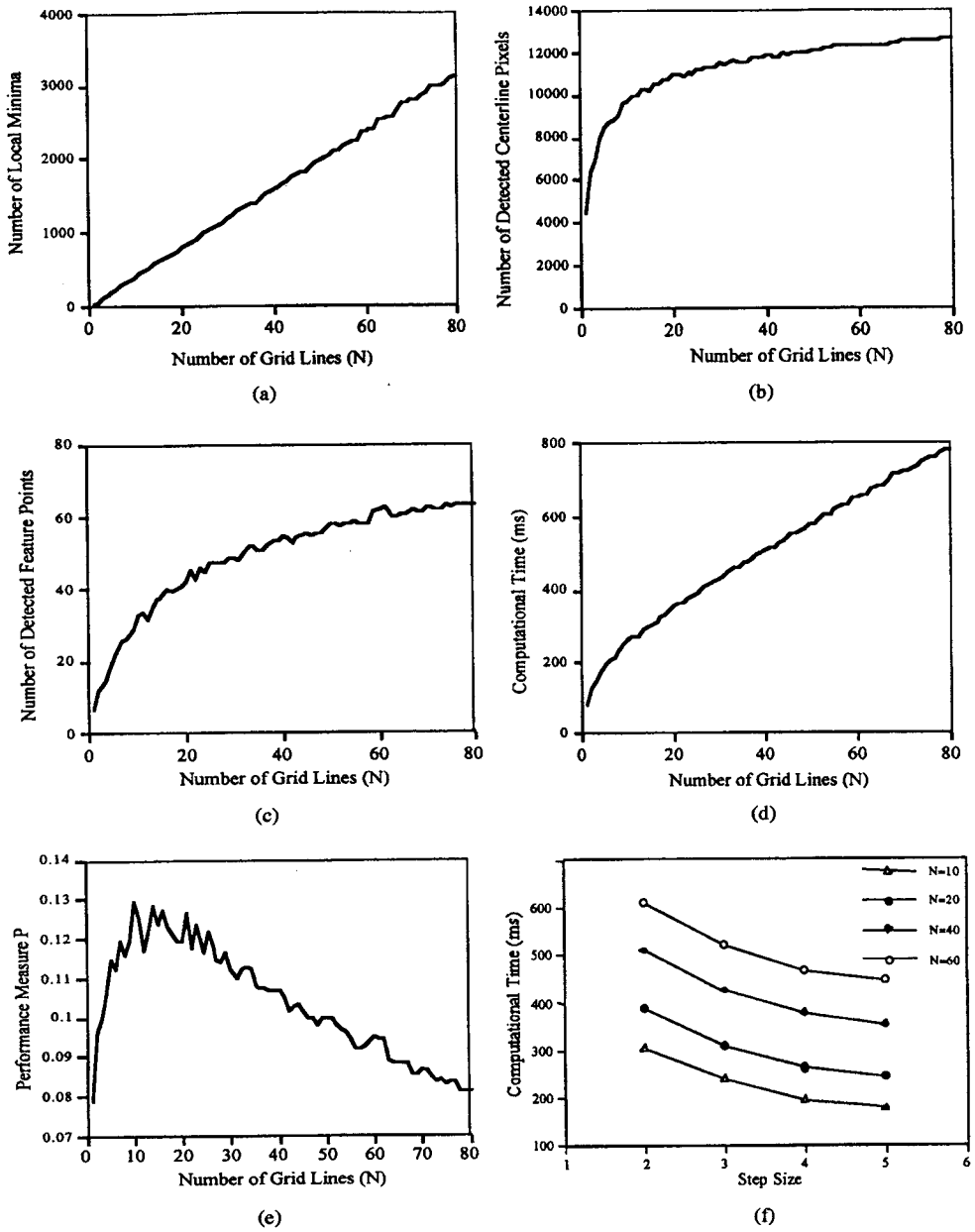

Fig. 5. Tradeoff between computation and detection performance for 10 frames. (a) Number of grid lines N versus the detected local minima, (b) N versus detected centerline pixels, (c) N versus detected feature points, (d) N versus computational time, (e) N versus performance measure P, and (f) step size versus computational time for different N values.

are checked in the order indicated above and the verification process is terminated if any one of the rules fail. The 22.5° tolerance rule is needed to account for quantization effects and small vessel curvatures. After the point is verified as a good seed point, the initial pair of opposite directions s_1^0 and s_2^0 are selected based on the maximum template responses, where s_1^0 is the direction corresponding to the highest response at the first peak between the left and right templates, and s_2^0 is the direction corresponding to the highest response at the second peak between the left and right templates. The tracing algorithm is initiated twice, starting from point $\vec{p}^0$, once in direction s_1^0, and once along s_2^0.

Fig. 2(b) illustrates the effectiveness of the above rules in detecting valid points on the vasculature, when implemented on all the pixels in Fig. 2(a). Clearly, the procedure succeeds in extracting the straight portions of all the vessels. However, for branching points, the templates have high outputs in more than two directions, so they do not satisfy the above rules, which can be seen in Fig. 2(b). On close inspection, many of the points that were apparently detected over the background were found to actually correspond to minute vessels, possibly from the choroid. The remaining points (and some of the misses over vessels) are due to noise. Overall, it is obvious that the above rules constitute an effective filtering mechanism. In order to illustrate the impact of the false detections in Fig. 2(b) on tracing performance, the algorithm was initiated at each of the validated points in Fig. 2(b). It was found that the algorithm would terminate rapidly for the false detections. The validated points that resulted in more than 10 tracing iterations are indicated in Fig. 2(c). The region highlighted by the rectangle

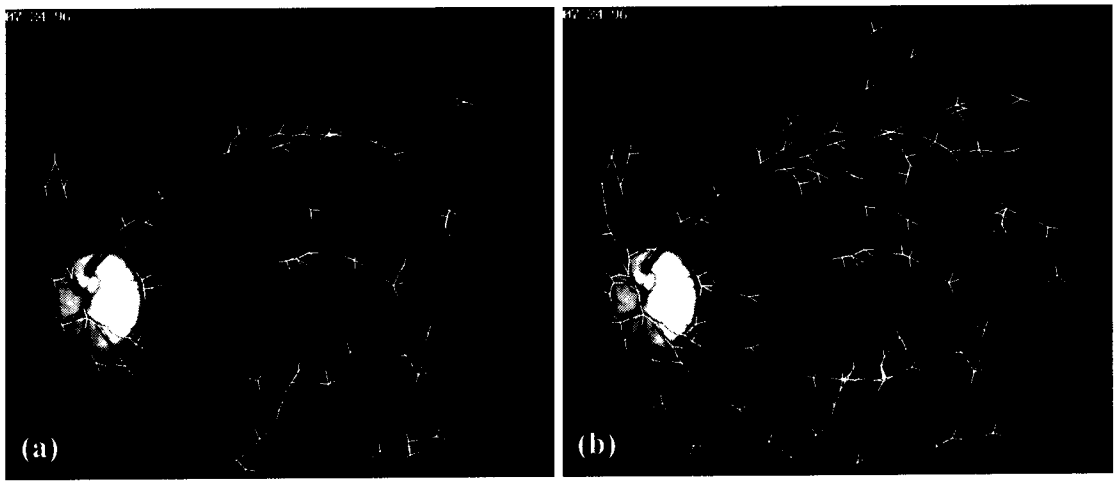

Fig. 6. The detected feature points for the image in Fig. 1(a) for grid sizes (a) 10 and (b) 60, respectively.

[shown enlarged in Fig. 2(d)] deserves additional comment. It shows a vessel that appears "hollow," which can occur, albeit rarely. Although many of the points on this segment failed to satisfy the validation rules, if any other point on the same vessel is validated, then the tracing algorithm is able to handle this type of area and will continue to follow either one of the darker edges. Another area where some incorrect initial points are found is near the optic disk. The change of illumination in this area looks like a vessel and the templates validate and track these points. As long as the same illumination characteristic is observed in all the images, this is a negligible problem for image matching, because consistent feature points are extracted in all the images.

F. Methods for Preventing Repetitious Tracing and Handling Vessel Intersections

All the detected centerline pixels are stored in two data structures. One is an integer array that has the same dimensions as the processed image and is called the "centerline image." This array is initialized to zero before any tracing begins. This operation can be carried out quickly, noting that only the values that were set for the previous image frame need to be reset for a new frame. As the tracing proceeds, the traced centerline of the vessel are set to a nonzero value. Specifically, as each new segment in the vasculature is tracked, we increment a variable called the "segment number." Before the validation rules described in the previous section are applied to one of the local intensity minima shown in Fig. 2(a), the centerline image is checked to see if the corresponding vessel has already been traced starting from another point. Now, since small spatial errors of the order of a few pixels may occur in the location of the centerline, the centerline image is checked on the boundary of a small square (of size 5×5 pixels) centered at the proposed initial location for the tracing. Since the vessels are continuous line segments, there is no need to check all the points inside the square; only the boundary pixels are sufficient. The centerline image is also used to detect previously detected vessels during the tracing process itself. As described earlier, the tracing algorithm only searches over the current and adjacent directions. Accordingly, three small line searches (2α pixels in length) are initiated from the current point $\vec{p}^k$ one in each of these three directions over the centerline image. If any of these searches encounters a nonzero value in the centerline image, then an intersection is inferred.

While the centerline image is an efficient data structure for detecting intersections as noted above, it is inefficient for higher level feature extraction. Therefore, a second compact data structure, called the "centerline network," consisting of a linked list of segments, is used. Each segment is a linked list of connected pixels representing the detected centerline of a vessel segment. When a previously detected vessel is intersected, the coordinate of the intersection point is searched in the corresponding point list of the centerline network, and it is updated. Two details worth noting are: 1) when a vessel is found to intersect with itself, the data structure is not split and 2) whenever a tracked segment is shorter than a fixed threshold L_p (typically 10α), it is simply rejected.

G. Extraction of Branching and Crossover Points

The branching and crossover points can be detected and characterized efficiently from the centerline network. Also of interest for matching problems are the "signatures" of these points. The signature of a feature point is simply the set of angles between the segments [1]. For each intersection point, the corresponding segment numbers are noted. Then, lines are drawn from the intersection point to points on the segments a fixed curved distance along the segment (18 pixels long). The slopes of these lines are used as estimates of the angles. If multiple intersections are located close to each other, they are combined and replaced by their centroid. The lines described above are then drawn from this centroid point. Fig. 6 shows all the feature points that are detected in Fig. 2(a). The angles between the vectors are invariant under rotation, scaling, and translation of the image. While the feature points can be used for estimating the motion (rotation, scaling, translation) of the eye between the frames of retinal images, the signature of the feature points gives the correspondences between the

feature point sets of the images. Pairing only the feature points with similar angles between two images decreases the computational time for motion estimation and increases the reliability of the system [1].

H. Settings and Adaptive Parameter Estimation

The parameters for the tracing and initialization algorithms are the grid size N, the neighborhood size N_s, the sensitivity threshold T, the step size α, the constant ρ in (13), the maximum expected vessel width M window size for testing if a seed point is on a previously detected vessel, and the minimum expected vessel length L_p. In Section III-E, we showed how N_s could be tied down to the maximum expected vessel width. Similarly, the minimum expected vessel length is closely related to the algorithm step size α. Indeed, it makes sense to reject any vessel segments that are shorter than a convenient fixed multiple of step sizes. Accordingly, we have set L_p to 10α in our work. This is also the minimum number of tracing iterations for a trace to be accepted. This parameter can be varied considerably without affecting the results significantly.

Increasing the grid size N improves the probability of detecting vessels at the expense of computation. Fig. 5(a) shows the nearly linear relationship between the number of detected local minima and the grid size. The graph in Fig. 5(b) demonstrates improved detection of vessels, as measured by the number of detected centerline pixels, as a function of the grid size. The rapid increase for small values of N (less than 6) can be mostly attributed to the thick and long vessels. The subsequent slower increase and leveling off is mostly due to the secondary and tertiary vessels. Fig. 5(c), which plots the number of feature points detected, denoted F, as a function of grid size exhibits a corresponding increase. The improved detection performance noted above entails increased computation. Fig. 5(d) plots the computational time, denoted T_{comp}, of the algorithm for the same image (not including the time for reading/writing). For increasing N, the number of the initial points that are checked for verification increases and the new vessel segments are traced, hence the computational time increases. A simple method to tradeoff computation and feature detection performance is to consider the ratio of F, and the computation time T_{comp}, as an overall performance measure. Fig. 5(e) plots this ratio, denoted P, as a function of the grid size. This graph exhibits a broad peak between 10 and 30, indicating that for grid sizes in this range, the cost-performance tradeoff is reasonable. For the computer hardware available to us (150 MHz SGI Indy), N was chosen as 10, which yields an average computation time of about 200 ms. The above performance measure may be refined/customized further. For instance, one may want to consider the reliability of each feature point itself. Those corresponding to primary vessels are more reliable compared to the ones on the secondary and tertiary vessels. Furthermore, the above measure is strongly influenced by image matching problems. Finally, the computation time is machine-dependent. Machine-independent measures of computational burden such as worst-case complexity are not particularly useful since the images vary greatly and the computation times vary accordingly.

Another parameter is the step size α. If α is too large, the centerline becomes jagged and the estimated next point can easily occur outside the vessels, especially for the minute vessels, since directions are quantized to only 16 values. In this case, the tracing algorithm would terminate prematurely, and, if the rest of the vessel is detected by a different initial point, false feature points may be obtained. On the other hand, small values of α result in more accurate tracing at the expense of more computation. Fig. 5(f) plots the computational time as a function of α. In our experience, the values of $\alpha = 3$ for high-resolution (1024×1024 pixels) images and $\alpha = 2$ for video-resolution (640×480 pixels) images represent acceptable tradeoffs.

The threshold T must be estimated for each new frame. This parameter is used in (11) to define the stopping criterion for the tracing, in (12) to prevent the tracing algorithm from jumping to a nearby vessel, and in Step 6) of the procedure for validation of initial points prior to invoking the tracing algorithm. An examination of the template design (Fig. 3) reveals that, neglecting quantization errors, the response of the left/right templates to a single unit of difference in background and foreground gray levels is 18. So, the minimum value of T should be 36, corresponding to a contrast of just one gray level. At the other extreme, T must never exceed 36 times the maximum gray-level value. An efficient estimation of T may be made based on the grid analysis step, which performs a sampling across the image. The local minima on the grid lines are points with a high probability of being on vessels, so the average gray-level value at the local minima is a good estimate for the average gray-level intensity of the vessels L_{av}. Complimentarily, the average gray level of the image background, denoted B_{av}, can be estimated from the remaining points on the grid lines. The contrast in the image frame is estimated as the absolute difference between the foreground and background estimates. Accordingly, T is set as follows:

$$T = 36(1 + \sigma|L_{\text{av}} - B_{\text{av}}|) \tag{14}$$

where σ is a scaling factor whose value lies between 0 and 1 and can be thought of as a percentage of the average contrast. Low values of σ makes the tracing more sensitive to noise and quantization errors. High values of σ make it terminate prematurely. This effect is illustrated in Fig. 7(a)–(d) in which the tracing algorithm was initiated from the same starting point for various values of T. The length of the traced segment is plotted in Fig. 12(e) **[Author: There is no Fig. 12(e) in this paper. Please clarify and revise.—Ed.]**. For reference, this segment was also traced manually. The manually measured length of the vessel was 251 pixels. Values of the sensitivity parameter between 5%–55% give traced lengths close to 251 pixels, indicating the robustness of this method. The result of running the tracing algorithm on the image in Fig. 2(a) using a σ value in this range (21%) is shown in Fig. 8(a)–(c).

IV. Experimental Results

The images were captured using a TOPCON TRC-50IA fun-

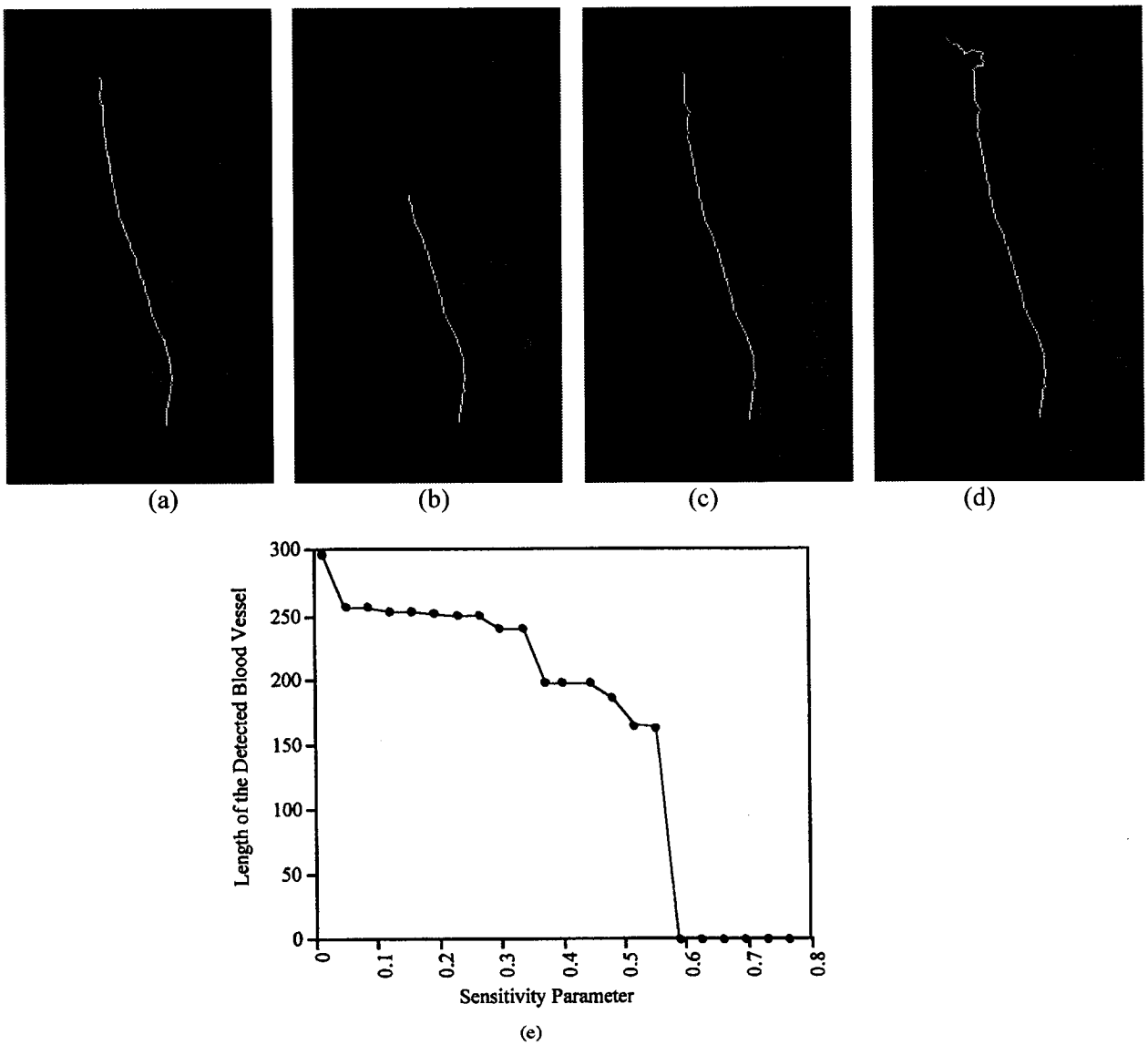

Fig. 7. Illustrating the impact of σ for a sample image. (a) Manually traced result (251 pixels). (b)–(d) Automatic tracing result starting at the same location at the bottom, and with σ of 5%, 21%, and 55%, respectively. (e) Sensitivity parameter versus detected length of a vessel segment.

dus camera using red-free illumination, and a Kodak Megaplus 1.4 CCD sensor attached to the top. The acquired images were at a resolution of 1024 × 1024 using the Topcon Imagenet H-1024 digital imaging software. The images were of fully dilated healthy as well as pathological eyes. The patients were allowed to move their eyes freely. The static high-resolution images were captured regardless of visual quality to simulate live imaging.

Fig. 8 presents the tracing results on one healthy eye under various imaging conditions and settings (a)–(f), and six pathological eyes (g)–(l). The latter is a subset of our much larger collection. Specifically, panels (a)–(c) show the results of setting the grid size N to 10, 20, and 60, respectively. In these frames, the correct algorithm-generated traces are presented as lines, the traces that were missed by the algorithm are manually traced, and indicated as black lines, and those that were algorithm-generated but clearly incorrect are presented as dotted lines. Clearly, increasing N leads to improved detection of the secondary and tertiary vasculature segments. It must be noted that, even for the lower value of grid size, the main vessels are detected successfully. Panels (d)–(l) show examples of tracing on low-quality and pathologic frames. The algorithm is able to adapt remarkably well to small amounts of defocus and significant changes in illumination level. Fig. 6(a) and (b) shows the increased number of feature points when the grid size is increased from 10 to 60.

V. Conclusions

This work has resulted in refinement and successful adaptation of exploratory tracing methods to live ophthalmic images. These images differ from X-ray images in that they are darker, have lower contrast in the region of most interest (the fovea), have higher signal-to-noise ratio, and are affected by different noise factors—frequent improper illumination, glare, fadeout, overexposure, loss of focus, motion, and artifacts arising from curvature, reflection, refraction, and dispersion.

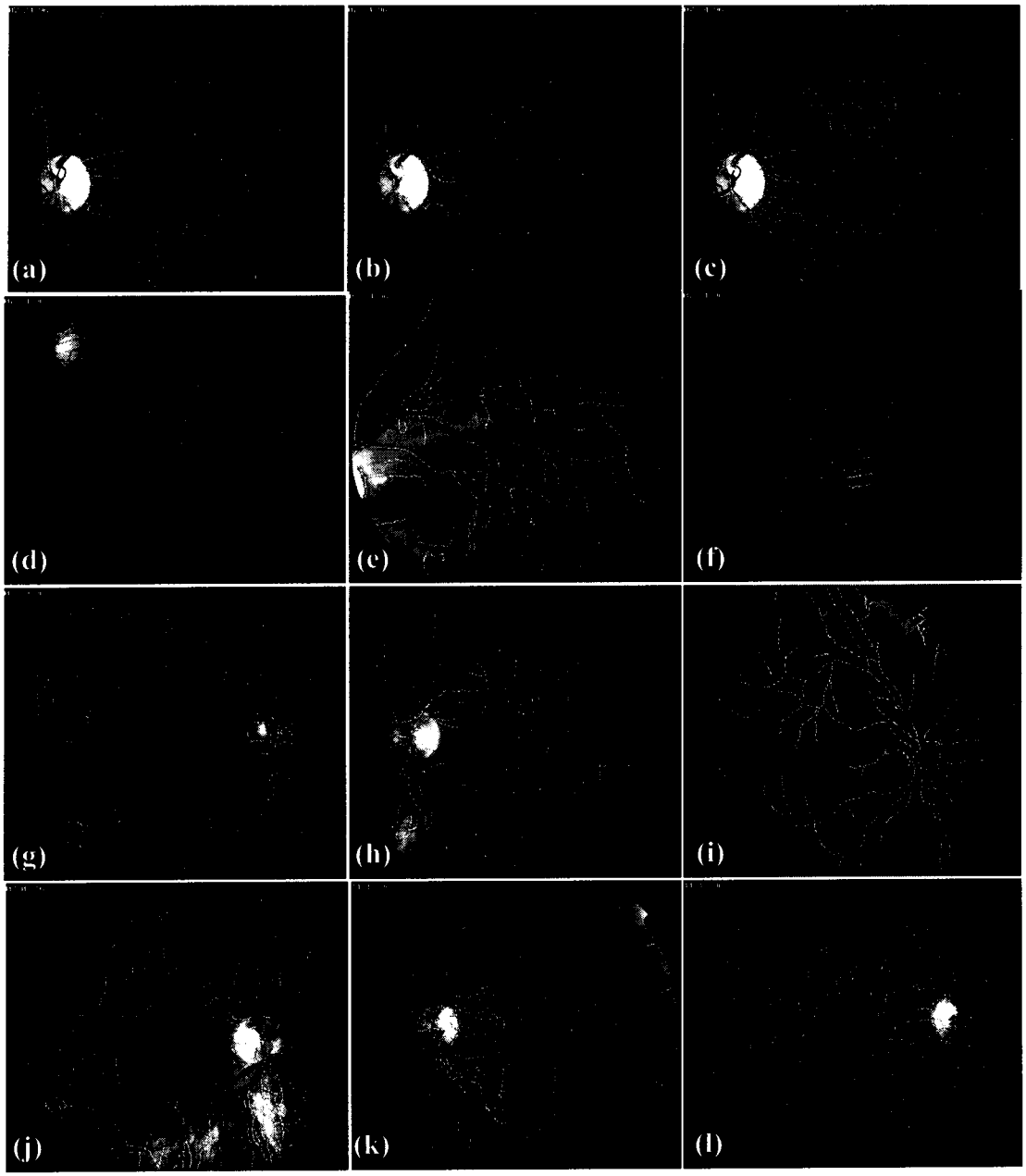

Fig. 8. Sample results on low- and high-quality frames. (a)–(c) Fig. 1(a) traced with grid sizes 10, 20, and 60, respectively, with other parameters the same. The correct traces are shown as white lines, traces that were missed are manually traced in black, and incorrect traces are shown as dotted lines.

Our algorithm improves upon cited works in terms of speed, automation, robustness, freedom from artifacts, and robust analysis of branches and crossovers in the specific context of ophthalmology. The design of our algorithm was driven by computational considerations as much as by detection performance. All computations can be implemented in fixed-point arithmetic, and the templates was based on a search in discrete space for computationally advantageous approximations to the ideal values. To illustrate, we implemented the Sobel edge detector on the images presented in Fig. 1 of this paper on the same computer that was used to generate the timing results in Fig. 5, using the same compiler settings. When just the square of Sobel magnitude was computed, i.e., without the square root operation, and without the trigonometric operations to compute the edge angles, it required an average of 440 ms for the 1024 × 1024 size images. Comparing this with the timing results in Fig. 5(f) illustrates the computational efficiency of the proposed exploratory algorithm relative to pixel-processing methods. The experiments indicate that the parameters that do need to be specified can all be specified approximately without appreciable impact.

VI. Discussion

The proposed algorithm is amenable to a variety of serial and parallel implementations. For instance, a dual-processor SGI workstation (Octane, with 180 MHz R10 K processors)

implementation yielded an average time of 30 ms per video frame by simply tiling the image into two blocks and pooling the results. It is also possible to assign a separate processor to each tracing thread, although this would involve the use of the centerline image as a shared memory area. Furthermore, the core tracing algorithm can be parallelized at finer levels. For instance, one could compute the left and right template responses in parallel and, additionally, compute template responses at multiple angles in parallel. Finally, the intratemplate computations can themselves be parallelized on pipelined or long-instruction word processors.

The algorithms presented here are being used to construct a computer-assisted instrument for laser retinal surgery [1], similar to the description given by Welch and his colleagues [38]–[42]. Recently, we have published an algorithm for real-time retinal tracking and location determination for video-resolution images [1]. This algorithm is based on using the point templates of Barrett *et al.* [39], [42] for small movements at a fixed magnification, and a slower matching procedure (800 ms) to reestablish tracking whenever the point templates fail, which occurs whenever low-quality frames are encountered, whenever the magnification is adjusted, and whenever the system is being started for the first time. Though effective, our earlier method had a disadvantage relating to the procedure for reestablishing tracking. It required extensive low-level pixel processing. This prompted an investigation of better scaling methods, leading to the exploratory methods reported here. *With the present formulation, in combination with the point templates of Barrett et al., it is possible to perform all the computations for the surgery system in an exploratory manner.* The exploratory approach is computationally more attractive (250 ms versus 800 ms) and scales better with image size. It also yields more compact signatures for the crossover and branching points [1]. It must be noted that the tracing algorithm is only invoked when the point templates [39]–[42] fail. When this occurs, the present algorithm is constantly applied to new frames, and a tracking lock is attempted until it succeeds. In this context, it is *not essential,* although desirable, for the tracing algorithm presented in this paper to operate at 30 frame/s. As noted earlier, this has been achieved for video-resolution image streams.

ACKNOWLEDGMENT

The authors would like to thank the staff at the Center for Sight, especially photographers G. Howe and M. Fish, for assisting with image acquisition. The authors appreciate the insightful inputs of Dr. G. Nagy at Rensselaer Polytechnic Institute, especially regarding vectorization methods from the document image analysis literature. Finally, the authors give many thanks to K. Al-Kofahi for various valuable inputs and to E. Balduf for the dual-processor frame-rate video-based implementation.

REFERENCES

[1] D. E. Becker, A. Can, H. L. Tanenbaum, J. N. Turner, and B. Roysam, "Image processing algorithms for retinal montage synthesis, mapping, and real-time location determination," *IEEE Trans. Biomed. Eng.*, vol. 45, **[Author: Please provide page numbers.—Ed.]**Jan. 1998.

[2] A. A. Mahurkar, M. A. Vivino, B. L. Trus, E. M. Kuehl, M. B. Datiles, III, and M. I. Kaiser-Kupfer, "Constructing retinal fundus photomontages," *Investigative Ophthalmology & Visual Science*, vol. 37, no. 8, pp. 384–401, pp. 1675–1683, July 1996.

[3] M. H. Goldbaum, N. Katz, S. Chaudhuri, M. Nelson, and P. Kube, "Digital image processing for ocular fundus images," *Ophthalmol. Clin. N. Amer.*, vol. 3, no. 3, pp. 447–466, Sept. 1990.

[4] M. H. Goldbaum, V. Kouznetsova, B. L. Coté, W. E. Hart, and M. Nelson, "Automated registration of digital ocular fundus images for comparison of lesions," *SPIE: Ophthalmic Technologies III*, vol. 1877, pp. 94–99, 1993.

[5] T. M. Clark, W. R. Freeman, and M. H. Goldbaum, "Digital overlay of fluorescein angiograms and fundus images for treatment of subretinal neovascularization," *Retina—The Journal of Retinal and Vitreous Diseases*, vol. 2, no. 12, pp. 118–126, 1992.

[6] S. Chaudhuri, S. Chatterjee, N. Katz, M. Nelson, and M. Goldbaum, "Detection of blood vessels in retinal images using two-dimensional matched filters," *IEEE Trans. Med. Imag.*, vol. 8, pp. 263–269, Sept. 1989.

[7] K. Stromland, A. Hellstrom, and T. Gustavsson, "Morphometry of the optic nerve and retinal vessels in children by computer-assisted image analysis of fundus photographs," in *Graefe's Arch. Clin. Exp. Ophthalmol.* Berlin, Germany: Springer-Verlag, 1995, vol. 233, pp. 150–153.

[8] R. Polli and G. Valli, "An algorithm for real-time vessel enhancement and detection," *Comput. Meth. Programs Biomed.*, vol. 52, pp. 1–22, 1997.

[9] A. S. Stansfield, "ANGY: A rule-based expert system for automatic segmentation of coronary vessels from digital subtracted angiograms," *IEEE Trans. Pattern Anal. Mach. Intell.*, vol. PAMI-8, pp. 188–199, Mar. 1986.

[10] J. Y. Catrox and D. Mischler, "An artificial intelligence approach for medical picture analysis," *Pattern Recogn. Lett.*, vol. 8, pp. 123–130, 1988.

[11] G. Coppini, M. Demi, R. Poli, and G. Valli, "An artificial vision system for X-ray images of human coronary trees," *IEEE Trans. Pattern Anal. Mach. Intell.*, vol. 15, pp. 156–162, Feb. 1993.

[12] J. L. Coatrieux, M. Garreau, R. Collorec, and C. Roux, "Computer vision approaches for the three-dimensional reconstruction: Review and prospects," *Critical Rev. Biomed. Eng.*, vol. 22, no. 1, pp. 1–38, 1994.

[13] L. H. Staib and J. S. Duncan, "Boundary finding with parametrically deformable models," *IEEE Trans. Pattern Anal. Machine Intell.*, vol. 14, **[Author: Please provide page numbers.—Ed.]**Nov. 1992.

[14] L. Zhou, M. S. Rzeszotarski, L. J. Singerman, and J. M. Chokreff, "The detection and quantification of retinopathy using digital angiograms," *IEEE Trans. Med. Imag.*, vol. 13, pp. 619–626, Dec. 1994.

[15] Y. Sun, "Automated identification of vessel contours in coronary arteriograms by an adaptive tracking algorithm," *IEEE Trans. Med. Imag.*, vol. 8, pp. 78–88, Mar. 1989.

[16] P. J. H. van Cuyck, J. J. Gerbrands, and J. H. C. Reiber, "Automated centerline tracing in coronary angiograms," *Pattern Recog. Artificial Intell.*, pp. 169–183, 1998.

[17] M. A. T. Figueiredo and J. M. N. Leitao, "A nonsmoothing approach to the estimation of vessel contours in angiograms," *IEEE Trans. Med. Imag.*, vol. 14, pp. 162–172, Mar. 1995.

[18] M. Sonka, M. D. Winniford, and S. M. Collins, "Reduction of failure rates in automated analysis of difficult images: Improved simultaneous detection of left and right coronary borders," *Computers in Cardiology*, pp. 111–114, 1992.

[19] M. Sonka, M. D. Winniford, and S. M. Collins, "Coronary borders in complex images," *IEEE Trans. Med. Imag.*, vol. 14, pp. 151–161, Mar. 1995.

[20] M. Sonka, M. D. Winniford, X. Zhang, and S. M. Collins, "Lumen centerline detection in complex coronary angiograms," *IEEE Trans. Biomed. Imag.*, vol. 41, pp. 520–528, June 1994.

[21] A. Klein, T. K. Egglin, J. S. Pollak, F. Lee, and A. A. Amini, "Identifying vascular features with orientation specific filters and B-spline snakes," *Computers in Cardiology*, **[Author: Please provide volume number.—Ed.]**pp. 113–116, 1994.

[22] M. Hart and L. Holley, "A method of automated coronary artery tracking in unsubtracted angiograms," *Computers in Cardiology*, **[Author: Please provide volume number.—Ed.]**pp. 93–96, 1993.

[23] E. Mortensen, B. Morse, W. Barrett, and J. Udupa, "Adaptive boundary detection using live-wire two-dimensional dynamic programming," *Computers in Cardiology*, **[Author: Please provide volume number.—Ed.]**pp. 635–638, 1992.

[24] Y. Liu and Y. Sun, "Recursive tracking of vascular networks in angiograms based on detection-deletion scheme," *IEEE Trans. Med.*

Imag., vol. 12, pp. 334–341, June 1993.
[25] S. Lu and S. Eiho, "Automatic detection of the coronary arterial contours with sub-branches from an X-ray angiogram," *Computers in Cardiology*, pp. 575–578, 1993.
[26] R. Collorec and J. L. Coatrieux, "Vectorial tracking and directed contour finder for vascular network in digital subtraction angiography," *Pattern Recog. Lett.*, vol. 8, no. 5, pp. 353–358, Dec. 1988.
[27] T. V. Nguyen and J. Sklansky, "Computing the skeleton of coronary arteries in cineangiograms," *Computers and Biomedical Research*, vol. 19, pp. 428–444, 1986.
[28] ——, "A fast skeleton-finder for coronary arteries," in *Proceedings Int. Conf. Pattern Recog.*, Paris, France, 1986, pp. 481–483.
[29] T. Fukui, M. Yachida, and S. Tsuji, "Detection and tracking of blood vessels in cine-angiograms," in *Proc. 5th Int. Conf. Pattern Recog.*, 1980, pp. 59–64.
[30] P. H. Eichel, E. J. Delp, K. Koral, and A. J. Buda, "A method for a fully automatic definition of coronary arterial edges from cineangiograms," *IEEE Trans. Med. Imag.*, vol. 7, pp. 313–320, Dec. 1988.
[31] H. Shen, "Optical instrumentation and real-time image processing algorithms for simultaneous ICG and red-free video angiography of the retina," M.S. thesis, Rensselaer Polytechnic Inst., Troy, NY, 1996.
[32] R. W. Flower and B. F. Hochheimer, "A clinical technique and apparatus for simultaneous angiography of the separate retinal and choroidal circulation," *Investigative Ophthalmology*, vol. 12, no. 4, pp. 248–261, Apr. 1973.
[33] R. D. T. Janssen and A. M. Vossepoel, "Adaptive vectorization of line drawing images," *Computer Vision and Image Understanding*, vol. 65, no. 1, pp. 38–56, Jan. 1997.
[34] M. Garreau, J. L. Coatrieux, R. Collorec, and C. Chardenon, "A knowledge-based approach for 3-D reconstruction and labeling of vascular networks from biplane angiographic projections," *IEEE Trans. Med. Imag.*, vol. 10, pp. 122–131, June 1991.
[35] L. V. Tran, R. C. Bahn, and J. Sklansky, "Reconstructing the cross sections of coronary arteries from biplane angiograms," *IEEE Trans. Med. Imag.*, vol. 11, pp. 517–529, Dec. 1992.
[36] T. V. Nguyen and J. Sklansky, "Reconstructing the 3-D medical axes coronary arteries in single-view cineangiograms," *IEEE Trans. Med. Imag.*, vol. 13, pp. 61–73, Mar. 1994.
[37] Y. Sun, R. J. Lucariello, and S. A. Chiaramida, "Directional low-pass filtering for improved accuracy and reproducibility of stenosis quantification in coronary arteriograms," *IEEE Trans. Med. Imag.*, vol. 14, **[Author: Please provide page numbers.—Ed.]**June 1995.
[38] A. J. Welch, "University of Texas lab studies tissue optics, ablation, automation," *Biomedical Optics: The Newsletter of the Biomedical Opt. Soc.*, vol. 2, no. 2, May 1993.
[39] S. F. Barrett, M. R. Jerath, H. G. Rylander, and A. J. Welch, "Digital tracking and control of retinal images," *Opt. Eng.*, vol. 33, no. 1, pp. 150–159, Jan. 1994.
[40] C. H. G. Wright, R. D. Ferguson, H. G. Rylander, III, A. J. Welch, and S. F. Barrett, "Hybrid approach to retinal tracking and laser aiming for photocoagulation," *J. Biomed. Opt.*, vol. 2, no. 2, pp. 195–203, Apr. 1997.
[41] S. F. Barrett, M. R. Jerath, H. G. Rylander, III, and A. J. Welch, "Automated lesion placement in the rabbit eye," *Lasers in Surgery and Medicine*, vol. 17, pp. 172–177, 1995.
[42] M. S. Markow, H. G. Rylander, and A. J. Welch, "Real-time algorithm for retinal tracking," *IEEE Trans. Biomed. Eng.*, vol. 40, no. 12, pp. 1269–1281, Dec. 1993.

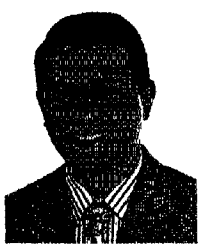

Ali Can received the B.S. degree in electrical engineering from the University of Gaziantep, Turkey, in 1993, and the M.S. degree in computer and engineering from Rensselaer Polytechnic Institute (RPI), Troy, NY, in 1997. He is currently working toward the Ph.D. degree at the same institution.

His research interests include biomedical image analysis and real-time applications, robust methods for motion, and structure estimation (2-D and 3-D) from image sequences.

Mr. Can is a member of the Microscopy Society of America.

Hong Shen received the B.Eng. degree in electrical engineering from Tsinghua University, China, in 1990, with concentration in optoelectronics and the M.Sc. degree in electrical engineering from Rensselaer Polytechnic Institute in 1996. He is currently working toward the Ph.D. degree in electrical and computer systems engineering.

From 1990 to 1994, he was a Research Engineer with the Institute of Semiconductors, Academic Sinica, China. His current research includes image analysis and processing, medical imaging, and instrumentation.

James N. Turner received the B.S. degree in engineering science in 1968, and the Ph.D. degree in biophysics in 1973, from the State University of New York at Buffalo.

He did National Institutes of Health and National Science Foundation postdoctoral fellowships at the Roswell Park Memorial Institute, Buffalo, NY. Currently, he is Director of the Three-Dimensional Light Microscopy Facility at the Wadsworth Center of the New York State Department of Health, Albany, NY. He is also Professor of Biomedical Engineering at Rensselaer Polytechnic Institute, Troy, NY, and Biomedical Sciences in the School of Public Health of the University at Albany. His interests focus on applications of light imaging methods and quantitative image analysis in biology and medicine, with special emphasis on the nervous system. He is on the editorial boards of *Microscopy and Microanalysis* and *Microscopy Research Techniques*, and has chaired numerous symposia in the area of 3-D microscopy, both light and electron, at meetings of the Microscopy Society of America.

Dr. Turner is a member of the Microscopy Society of America, the International Society for Analytical Cytology, AAAS, and the Society for Neuroscience. He frequently serves on National Institutes of Health advisory panels.

Howard L. Tanenbaum received the B.Sc. and M.D.C.M. degrees from McGill University, Canada.

He has taught ophthalmology at various levels at the University of Colorado, Fort Collins (1962 to 1963), Montreal General Hospital (1968 to 1969), Jewish General Hospital, Montreal, Canada (1968 to 1984), McGill University (1968 to 1984), and Albany Medical College, Albany, NY (1984 to 1987). He is currently director of The Center for Sight, Albany, NY. His research interests are in proliferative vitreoretinal diseases, diabetic retinopathy, neovascularization, and a variety of laser-related issues.

Dr. Tanenbaum is a Fellow of the Royal College of Physicians and Surgeons of Canada. He is a member of the Association for Research in Vision and Ophthalmology (ARVO), Canadian Medical Association, The Retina Society, the American Academy of Ophthalmology, the New York Academy of Science, the Quebec Retina Club, the Macula Society, the Northeast Eye, Ear, and Throat Society of New York, the New York State Medical Society, the New York State Ophthalmological Society, and The American Medical Association. He is on the editorial committee of the National Eye Trauma Registry and a contributing editor to the *Ophthalmic Practice Journal*.

Badrinath Roysam (M'89) received the B.Tech. degree in electronics engineering from the Indian Institute of Technology, Madras, India, in 1984, and the M.S. and D.Sc. degrees in electrical engineering from Washington University in St. Louis, MO, in 1987 and 1989, respectively.

He has been at Rensselaer Polytechnic Institute, Troy, NY, since 1989, where he is currently an Associate Professor in the Electrical, Computer, and Systems Engineering Department. He has consulted for various major and small corporations on imaging systems and image processing, and has assisted venture capital companies with a detailed analysis of startup companies. His current research interests are in the areas of biomedical image analysis, optical instrumentation, high-speed and real-time computing architectures, parallel algorithms, and compelling medical applications.

Dr. Roysam is a member of the Microscopy Society of America and the Association for Research in Vision and Ophthalmology.